Applications of Linear and Nonlinear Robustness Analysis Techniques to the F/A-18 Flight Control Laws

Abhijit Chakraborty * and Peter Seiler † and Gary J. Balas‡

Department of Aerospace Engineering & Mechanics, University of Minnesota , Minneapolis, MN, 55455, USA

The F/A-18 Hornet with the baseline control law exhibited an out-of-control phenomenon known as the falling leaf mode. Several aircraft were lost due to the falling leaf mode and this led NAVAIR and Boeing to redesign the control law. The revised control law successfully suppressed the falling leaf mode during flight tests with aggressive maneuvers. This paper compares the robustness of the baseline and revised control laws using linear analyses, Monte Carlo simulations, and nonlinear region-of-attraction analyses. The linear analyses indicate the revised controller only marginally improves the closed-loop robustness while the nonlinear analyses indicate a substantial improvement in robustness over the baseline controller. This example demonstrates the potential for nonlinear analyses to detect out-of-control phenomenon that are not indicated by classical linear analyses.

Nomenclature

α	Angle-of-attack, rad
β	Sideslip Angle, rad
V_T	Velocity, ft/s
p	Roll rate, rad/s
q	Pitch rate, rad/s
r	Yaw rate, rad/s
ϕ	Bank angle, rad
θ	Pitch angle, rad
ψ	Yaw angle, rad
T	Thrust, lbf
ρ	Density, slugs/ft^3
$\bar{q}$	$\frac{1}{2}\rho V_{TAS}^2$: Dynamic pressure
V	Lyapunov Function

I. Introduction

The US Navy F/A-18 A/B/C/D Hornet with the baseline control law has experienced many out-of-control flight departures since the early 1980's. Many of these incidents have been described as the falling leaf motion of the aircraft.[?] The falling leaf motion has been studied extensively to investigate the conditions that lead to this behavior. The complex dynamics of the falling leaf motion and lack of flight data from the departure events pose a challenge in studying this motion. An extensive revision of the baseline control law was performed in 2001 to suppress departure phenomenon, improve maneuvering performance and to expand the flight envelope.[?] The revised control law was implemented on the F/A-18 E/F Super Hornet after successful flight tests. These flight tests included aggressive maneuvers that demonstrated the succesful supression of the falling leaf motion by the revised control law.

*Graduate Research Assistant: chakrab@aem.umn.edu.

†Senior Research Associate: seile017@umn.edu.

‡Professor: balas@aem.umn.edu.

It is of practical interest to compare the robustness of the baseline and revised controllers. One major objective of this paper is to use linear analyses, Monte Carlo simulations, and nonlinear region-of-attraction analyses to compare these control laws. The region of attraction analysis provides a guaranteed stability region using Lyapunov theory and recent results in sum-of-squares optimization.[?] This is complementary to the use of Monte Carlo simulations to search for unstable trajectories. The sums-of-squares stability analysis has previously been applied to simple examples.[?] The second major objective of this paper is to apply this method to analyze and draw conclusions about a real flight control system. The falling leaf motion is due to nonlinearities in the aircraft dynamics and cannot be replicated in simulation by linear models. This makes the falling leaf motion a particularly interesting example for the application of nonlinear robustness analysis techniques.

The remainder of the paper has the following outline. Section II describes the characteristics of the falling leaf motion. Section III provides a brief description of the F/A-18 aircraft including its aerodynamic characteristics and equations of motion. The baseline and revised control laws are described in Section IV. Section V provides a comparison of the closed-loop robustness properties with the baseline and revised control laws. This section includes both the linear and nonlinear analyses for each control law. Finally a brief conclusion is given in Section VI. All data required to reproduce the results presented in this paper are provided in the Appendices.

II. Falling Leaf Motion

The falling leaf motion of an aircraft can be characterized as large, coupled out-of-control oscillations in the roll (p) and yaw (r) direction combined with large fluctuations in angle-of-attack (α) and sideslip (β).[?,?] Figure 1 shows the main characteristics of the falling leaf motion.[?,?] This out-of-control mode exhibits periodic in-phase roll and yaw rates with large amplitude fluctuations about small or zero mean. The roll and yaw rate generation is mainly due to the large sideslip oscillation. During large sideslip and angle-of-attack motion, the dihedral effect (roll caused by sideslip) of the aircraft wings becomes extremely large and the directional stability becomes unstable. The like-signs of these two values are responsible for the in-phase motion. The roll rate motion can easily reach up to $\pm 120°/s$, while the yaw rate motion can fluctuate around $\pm 50°/s$. During this motion, the value of angle-of-attack can reach up to $\pm 70°$ with sideslip oscillations between $\pm 40°$.[?] The required aerodynamic nose-down pitching moment is exceeded by the pitch rate generation due to the inertial coupling of the in-phase roll and yaw rates. The reduction in pitching moment is followed by a reduction in normal force, eventually causing a loss of lift in the aircraft. A distinguishing feature of the falling leaf motion is that α vs. β plot produces a mushroom shape curve as seen in Figure 1. For more details on the falling leaf motion, readers are encouraged to refer to the papers by Jaramillo & Ralston[?] and Heller, David & Holmberg.[?]

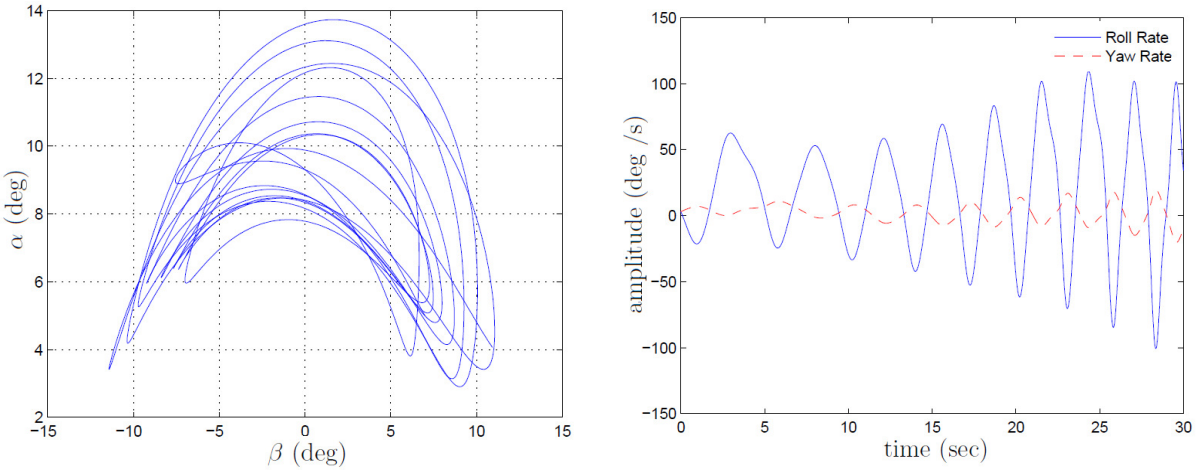

Figure 1. Characteristic Behavior of Falling Leaf Motion

III. F/A-18 Aircraft Description and Model Development

This section contains a brief description of the F/A-18 Hornet including the physical parameters and the aerodynamic characteristics of the aircraft. More information can be found in the report by Buttrill, Arbuckle, and Hoffler.[?] A full six degree-of-freedom (DOF) nonlinear model of the F/A-18 Hornet dynamics is presented in Appendix **??**. This full model is not directly used in any of the analyses presented in this paper and is included for completeness. Each of the analyses presented in this paper uses a slightly different approximated model derived from this full 6 DOF model. To avoid confusion, it is worth summarizing the various models which will be used. A six state, cubic order polynomial model is presented in Appendix **??**, is appropriate for the analysis of roll-coupled maneuvers. This cubic-order polynomial model was used to generate the falling leaf simulations shown in Figure 1 and for linearization about trim points. The resulting linear state space models, given in Appendix **??**, are used to perform the linear robustness analysis in Section **??**. The state space realizations of both the baseline and revised control laws are provided in Appendix **??**. For either control law, the closed loop system can be generated by placing the linear control law in Appendix **??** in negative feedback around the appropriate linear model in Appendix **??**. The nonlinear region of attraction analysis in Section 3.0.1 requires the closed loop system dynamics be described by a polynomial function of the states. Linear least squares techniques are used to approximate the closed loop systems with each control law. These polynomial models are provided in Appendix **??**. Figure 2 shows the steps pictorially that have been mentioned above. s

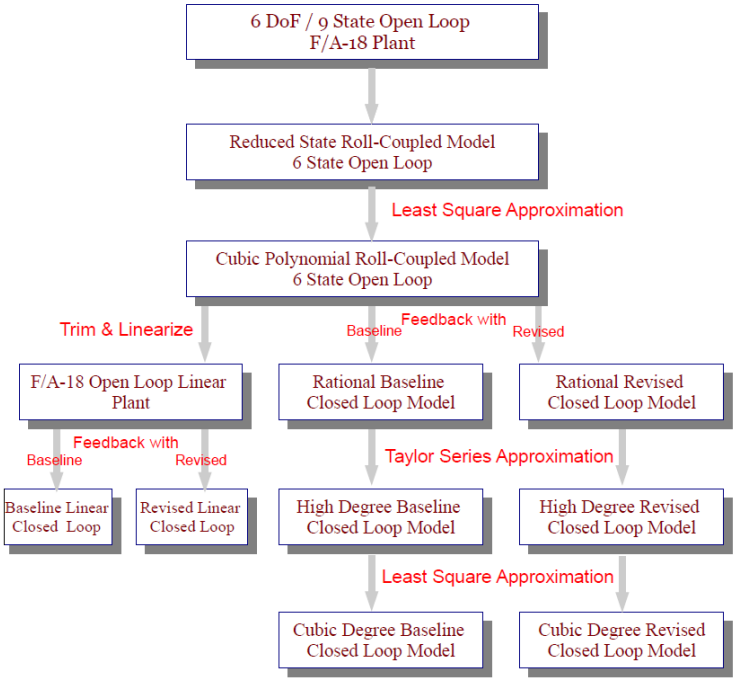

Figure 2. Steps for F/A-18 Model Reduction

As we proceed through the various analyses, we will again explicitly state the model being used in each case. In the remainder of this section, we provide a more general description of the F/A-18 dynamics.

A. Physical Parameters

The F/A-18 Hornet, Figure **??**[a], is a high performance, twin engine fighter aircraft built by the McDonnell Douglas (currently known as the 'Boeing') Corporation. Each engine is a General Electric, F404-GE-400 rated at 16,100-lbf of static thrust at sea level. The aircraft features a low sweep trapezoidal wing planform with 400 ft^2 area and twin vertical tails.[?] Table **??** lists the aerodynamic reference and physical parameters of the aircraft.

[a]Pictures taken from http://www.dfrc.nasa.gov/Gallery/Photo/F-18Chase/Large/EC96-43830-11.jpg

Figure 3. F/A-18 Hornet

Table 1. Aircraft Parameters

Wing Area, S_{ref}	400 ft^2
Mean Aerodynamic Chord (c)	11.52 ft
Wing Span, b_{ref}	37.42 ft
Weight	33310 lbs
I_{xx}	23000 slug-ft^2
I_{yy}	151293 slug-ft^2
I_{zz}	169945 slug-ft^2
I_{xz}	-2971 slug-ft^2

B. Control Surfaces

The conventional F/A-18 Hornet has five pairs of control surfaces: stabilators, rudders, ailerons, leading edge flaps, and trailing edge flaps. However, only the symmetric stabilator, differential aileron and differential rudder are considered as control effectors for the analysis performed in this paper. Longitudinal control or pitch control is provided by the symmetric deflection of the stabilators. Deflection of differential ailerons is used to control the roll or lateral direction, while differential deflection of rudders provide directional or yaw control. There is a coupling between roll and yaw dynamics. The actuation systems for these primary controls are modeled as first order lags. Table **??** provides the mathematical models of the actuators and their deflection and rate limits.[?]

Table 2. Control Surface and Actuator Configuration

Actuator	Rate Limit	Position Limit	Model
Stabilator	±40°/s	-24°,+10.5°	$\frac{30}{s+30}$
Aileron	±100°/s	-25°,+45°	$\frac{48}{s+48}$
Rudder	±61°/s	-30°,+30°	$\frac{40}{s+40}$

C. Equations of Motion & Aerodynamic Model

The conventional aircraft equations of motion described in Stengel,[?] Cook,[?] and Napolitano and Spagnuolo[?] are primarily driven by the aerodynamic forces and moments acting on the aircraft. In this paper, we follow the notation used in the report by Napolitano and Spagnuolo.[?] The equations of motion for the 6 DOF full model are presented in the Appendix **??**. The two aerodynamic angles, angle-of-attack (α) and sideslip angle (β), are needed to specify the aerodynamic forces and moments. These aerodynamic forces and moments also depend on the angular rates and the deflection of the control surfaces. The longitudinal coefficients (lift, drag, and pitching moment) primarily depend on the angle-of-attack (α); in the lateral directional coefficients

(roll, yaw, and sideforce), sideslip angle (β) is equally as important as α.[?] Many flight experimental have been performed to estimate the stability and control derivatives of the F/A-18 High Alpha Research Vehicle (HARV).[?,?,?,?] The F/A-18 HARV has similar aerodynamic characteristics as the F/A-18 Hornet[?] with the exception of the F/A-18 HARV having thrust vectoring control. Hence, we will use the F/A-18 HARV aerodynamic data to build up all the models that are presented in this paper. The aerodynamic model for the full six degree-of-freedom model is presented in the Appendix **??**.

D. Reduced Equations of Motion

The nonlinear region of attraction analysis[?] requires the aircraft dynamics to be described via polynomial model. The computational burden of the analysis tool also restricts the order of the dynamics up to cubic degree. Hence, a six state cubic degree polynomial model of the F/A-18 aircraft for roll-coupled maneuvers[?] is used in this paper for performing all the analyses. The reduced equations of motion, along with the reduced order approximated aerodynamic model, are presented in the Appendix **??**. The polynomial model described in the Appendix B captures the characteristics of the full 6 DOF model presented in Appendix **??**. This polynomial model is derived based on the characteristics of the falling leaf motion. During this OCF motion, the velocity is usually on the order of 250 ft/s.[?] In this paper, the velocity is assumed to be constant, and equal to 250 ft/s. Aggressive maneuvers, like bank turn, is more likely to put the aircraft in the falling leaf motion compare to the straight and level flight. Hence, we consider steady bank turn maneuver of the aircraft with zero climb rate ($\dot{\theta} = 0$). Now, we can ignore two other states: pitch angle (θ) and yaw angle (ψ), resulting in a six state model. Thrust effects in the sideslip direction is also neglected. Small angle approximations are used for the trigonometric terms in the full 6 DOF model to derive a polynomial representation of the aircraft dynamics. Finally, we perform least squares fit over a gridded α - β space of $-20^\circ \leq \beta \leq 20^\circ$, and $-10^\circ \leq \alpha \leq 40^\circ$ to restrict the description of the dynamics up to cubic degree.

E. Linear Models Formulation

The cubic degree polynomial model, presented in Appendix **??**, is linearized around steady ($\beta = 0$) and unsteady ($\beta \neq 0$) turning maneuvers for different bank angles (ϕ). Steady bank turn is an usual maneuver for any aircraft. However, wind disturbances or any upset conditions can force the aircraft to perform unsteady bank turn maneuvers. Hence, we will consider both scenarios. Aggressive maneuvers, like large bank turn (i.e, $\phi = 60^o$), is more likely to put the aircraft into the falling leaf motion compare to the straight and level flight. Longitudinal and lateral direction become highly coupled during such maneuvers. Hence, linearization around such maneuvers result in linear models which may be well suited to capture the characteristics of the highly nonlinear phenomenon like the falling leaf motion. Hence, it is of considerable interest to perform linear robustness comparison between the baseline and revised flight control law. The operating points for formulating the linear models are presented in Table **??**. All the plants are trimmed around the flight condition of: $V_T = 250$ ft/s, altitude $=25,000$ ft, and $\alpha = 26^o$.

Table 3. Trim Values

State/Input	Plant 1	Plant 2	Plant 3	Plant 4	Plant 5	Plant 6	Plant 7	Plant 8
Sideslip, β	0°	0°	0°	0°	10°	10°	10°	10°
Bank Angle, ϕ	0°	25°	45°	60°	0°	25°	45°	60°
Roll Rate, p	0°/s	0°/s	0°/s	0°/s	0°/s	0°/s	0°/s	0°/s
Yaw Rate, r	0°/s	3.20°/s	5.78°/s	7.70°/s	0.069°/s	3.28°/s	5.84°/s	7.77°/s
Pitch Rate, q	0°/s	0°/s	0°/s	0°/s	0°/s	0°/s	0°/s	0°/s
δ_{Stab}	-21.78°	-21.78°	-21.78°	-21.78°	-21.78°	-21.78°	-21.78°	-21.78°
δ_{Ail}	0°	0.31°	0.56°	0.75°	19.68°	19.98°	20.24°	20.42°
δ_{Rud}	0°	-2.37°	-4.27°	-5.69°	3.32°	0.96°	-0.94°	-2.36°
T (lbf)	36464	36464	36464	36464	36464	36464	36464	36464

IV. Control Law Design

This section provides an overview of both the baseline and revised control laws. In both cases, the control laws are divided into three channels: longitudinal, lateral, and directional.

A. Baseline Control Law

Figure **??** shows the control law architecture for the baseline control laws used for analysis in this paper. The baseline controller structure for the F/A-18 aircraft closely follows the *Control Augmentation System (CAS)* presented in the report by Buttrill, Arbuckle, and Hoffler.[?] The actuator ($A_{stab}, A_{rud}, A_{ail}$) dynamics, presented in Table **??**, are neglected for analysis purposes, i.e. $A_{stab} = A_{rud} = A_{ail} = 1$. Any differences between the control structure presented here and in the report by Buttrill, Arbuckle, and Hoffler[?] is described in the following sections.

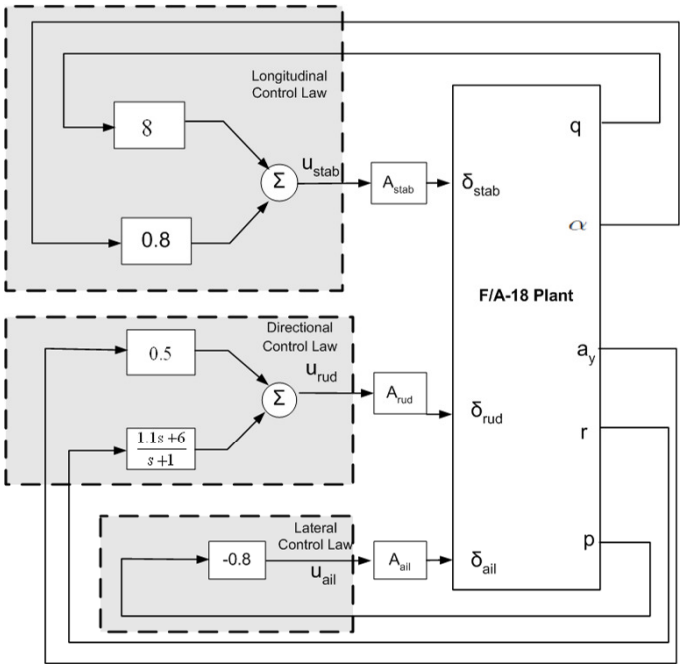

Figure 4. F/A-18 Baseline Flight Control Law

1. *Longitudinal Control*

The longitudinal baseline control design for the F/A-18 aircraft includes angle-of-attack (α in rad), normal acceleration (a_n, g), and pitch rate (q in rad/s) feedback. The angle-of-attack feedback is used to stabilize an unstable short-period mode that occurs during low speed, high angle-of-attack maneuvering. The inner-loop pitch rate feedback is comprised of a proportional feedback gain, to improve damping of the short-period mode. In the high speed regime, this feedback gain needs to be high to avoid any unstable short-period mode. The normal acceleration feedback, a proportional-integrator (PI) compensator, has not been implemented in our analysis since only roll-coupled maneuvers are considered. *WHY IGNORED?*

2. *Lateral Control*

Control of the lateral direction axis involves roll rate (p in rad/s) feedback to the aileron actuators. Roll rate feedback is used to improve roll damping and the roll-subsidence mode of the aircraft. Due to the inherent high roll damping associated with the F/A-18 aircraft at high speed, the roll rate feedback authority is usually reduced at high dynamic pressure. In the low speed regime, the roll rate feedback gain is increased to improve the Dutch roll damping. The roll rate feedback gain ranges between 0.8 at low speed to 0.08 at

high speed. At 250 ft/s and flight condition described in this paper, a feedback gain of 0.8 is used to provide roll damping.

3. Directional Control

Directional control involves feedback from yaw rate (r in rad/s) and lateral acceleration (a_y in g) to the rudder actuators. Yaw rate is fed back to the rudder to generate a yawing moment. Yaw rate feedback reduces yaw rate contribution to the Dutch-roll mode. In steady state turn, there is always a constant nonzero yaw rate present. This requires the pilot to apply larger than the normal rudder input to negate the effect of the yaw damper and make a coordinated turn. Hence, a washout filter is used to effectively eliminate this effect. The filter approximately differentiates the yaw rate feedback signal at low frequency, effectively eliminating yaw rate feedback at steady state conditions.[?] The lateral acceleration feedback contributes to reduce sideslip during turn coordination.

B. Revised Control Law

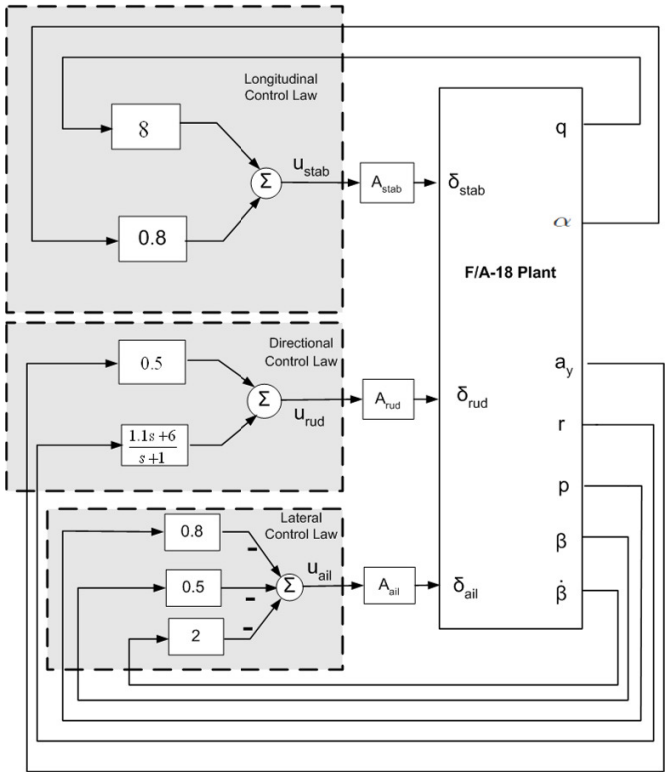

Figure 5. F/A-18 Revised Flight Control Law

Figure **??** shows the architecture of the revised F/A-18 flight control law and is described in the papers by Heller, David, & Holmberg[?] and Heller, Niewoehner, & Lawson.[?] The objective of the revised flight control law was to improve the departure resistance characteristics and full recoverability of the F/A-18 aircraft from all high angle-of-attack, OCF departure without sacrificing the maneuverability of the aircraft.[?] The significant change in the revised control law was the additional sideslip (β in rad) and sideslip rate ($\dot{\beta}$ in rad/s) feedback to the aileron actuators. The sideslip feedback plays a key role in increasing the lateral stability in the $30 - 35^{\circ}$ range of angle-of-attack. The sideslip rate feedback improves the lateral-directional damping. Hence, sideslip motion is damped even when the angle-of-attack is high. This feature is key to

eliminating the falling leaf mode, which is an aggressive form of in-phase Dutch-roll motion. There are no direct measurements of sideslip and sideslip rate, hence they are estimated for feedback. The sideslip and the sideslip rate feedback signals are computed based on already available signals from the sensors, probes and using the kinematics of the aircraft. Proportional feedback law has been implemented for these two feedback channels. The values of the proportional gains are $k_\beta = 0.5$ and $k_{\dot{\beta}} = 2$, respectively.

V. Analysis

Linear robustness and nonlinear region-of-attraction analyses are performed to compare the baseline and the revised F/A-18 flight control laws. The linear analysis captures the local behavior of the system and is only valid around the equilibrium point of the linearization. Linear analysis does not provide insight into how the nonlinearities of the aircraft dynamics will affect the stability properties of the system. Two approaches are taken to analyze the effect of the nonlinearities. First, the closed-loop flight control systems are analyzed by using region-of-attraction estimation techniques to compute an inner estimate of the stability boundaries. Second, Monte Carlo simulations are performed on the closed-loop dynamics to estimate outer bounds of the stability boundaries. The linear robustness analysis has been performed using the *Robust Control Toolbox*.[?]

A. Linear Analysis

The cubic order polynomial model described in Appendix **??** is linearized around the flight condition of: $V_{TAS} = 250$ ft/s, altitude $=25,000$ ft at different bank angle turn, i.e, $\phi = 0^o,\ 25^o,\ 45^o,\ 60^o$. Section **??** presents the operating points for the linear systems. The actuator states are excluded from both linear and nonlinear models. The actuators have very fast dynamics, as mentioned in Table **??**, and their dynamics can be neglected without causing any significant variation in the analysis results. Validation and verification of flight control law relies heavily on applying linear analysis at trim points throughout the flight envelope. Linear analysis usually amounts to investigating robustness issues and possible worst-case scenarios around the operating points of interest. These linear analytical methods are well developed and well understood.

B. Loopmargin Analysis

Gain and phase margins provide stability margins for the closed-loop system. Poor gain and phase margins indicate poor robustness of the closed-loop system. A typical requirement for certification of a flight control law requires the closed-loop system to achieve at least $6dB$ of gain margin and 45^0 of phase margin. However, the classical loop-at-a-time SIS0 (Single-Input-Single-Output) margin can be unreliable for MIMO (Multi-Input-Multi-Output) systems. The F/A-18 closed loop plants under consideration are MIMO; hence, we will perform both disk margin and multivariable margin analysis in addition to the classical loop-at-a-time margin analysis.

1. Classical Gain, Phase and Delay Margin Analysis

The classical gain, phase and delay margins provides stability margins for each individual feedback channel with all the other loops closed. This loop-at-a-time margin analysis provides some insight on the sensitivity of each channel individually. Table **??** provides the classical margins for both the baseline and the revised flight control laws. The results are based on the unsteady ($\beta \neq 0$) bank turn maneuvers at $\phi = 60^o$. The baseline and revised flight control laws have very similar classical margins at the input channel. However, loop-at-a-time margin analysis can be unreliable for MIMO system. Hence, multivariable loop margin analysis is necessary to decide on which control law has better stability margins.

2. Disk Margin Analysis

Disk margin provides an estimate on how much combined gain/phase variations can be tolerated at each channel with other loops closed. Hence, as with the classical margin calculation, coupling effects between channels may not be captured by this analysis. Table **??** provides the disk gain and phase variations at each loop for both the control laws. The results are based on the unsteady ($\beta \neq 0$) bank turn maneuvers at $\phi = 60^o$. The baseline flight control law achieves slightly better stability margins in the stabilator channel; while the revised flight control law has slightly better margins in the aileron channel. Overall, the disk margins

Table 4. Classical Gain & Phase Margin Analysis

Input Channel		**Baseline**	**Revised**
Aileron	*Gain Margin*	∞	27 dB
	Phase Margin	-110^o	93^o
	Delay Margin	1.30 sec	0.44 sec
Rudder	*Gain Margin*	34 dB	34 dB
	Phase Margin	77^o	76^o
	Delay Margin	2.21 sec	1.99 sec
Stabilator	*Gain Margin*	∞	∞
	Phase Margin	91^o	91^o
	Delay Margin	0.24 sec	0.62 sec

between the two flight control laws are nearly indistinguishable. Disk margin analysis has not provided any definitive certificate on which flight control law is more robust. The multivariable, simultaneous disk margin analysis across all channels may provide a better insight on which control law has better margins.

Table 5. Disk Margin Analysis

Input Channel		**Baseline**	**Revised**
Aileron	*Gain Margin*	27 dB	∞
	Phase Margin	85^o	90^o
Rudder	*Gain Margin*	15 dB	14 dB
	Phase Margin	69^o	67^o
Stabilator	*Gain Margin*	∞	51 dB
	Phase Margin	90^o	90^o

3. Multivariable Disk Margin Analysis

The multivariable disk margin indicates how much simultaneous (across channels), independent gain and phase variations can the closed-loop system tolerate before becoming unstable. This analysis is conservative since it allows independent variation of the input channels simultaneously. Figure **??** presents the multivaribale disk margin ellipses. The mutivariable disk margin analysis certifies that for simultaneous gain & phase variations in each channel inside the region of the ellipses the closed-loop system remains stable. The mutivariable disk margin analysis for steady bank turn maneuvers, in Figure **??** shows both the baseline and the revised flight control laws has similar multivariable margin. For this steady maneuver, both the control laws can handle gain variation up to ≈ 12.5 dB and phase variation of $\approx 64^o$ across channels. Figure **??** shows the mutivariable disk margin analysis for unsteady bank turn maneuvers. Here, the revised flight control law achieves slightly better margin (Revised: gain margin = $11.3dB$, phase margin = 60^0) than the baseline flight control law (Baseline: gain margin = $9.5dB$, phase margin = 54^0). However, the differences in the margins between the two control laws is not significant enough to conclude on which flight control law is susceptible to the falling leaf motion. Moreover, both the control laws achieve the typical margin requirement specification ($6dB$ gain margin and 45^0 phase margin).

C. Input Multiplicative Uncertainty

Modeling physical systems perfectly is always a challenge. A mathematical model of the physical system always differs from the actual behavior of the system in many engineering problems. The F/A-18 aircraft model presented in this paper is no exception. One approach is to account for the inaccuracies of the modeled aircraft dynamics as input multiplicative uncertainty.

Figure **??** shows the general uncertainty structure of the plant that will be considered in the input multiplicative uncertainty analysis. To assess the performance due to the inaccuracies of the modeled dynamics,

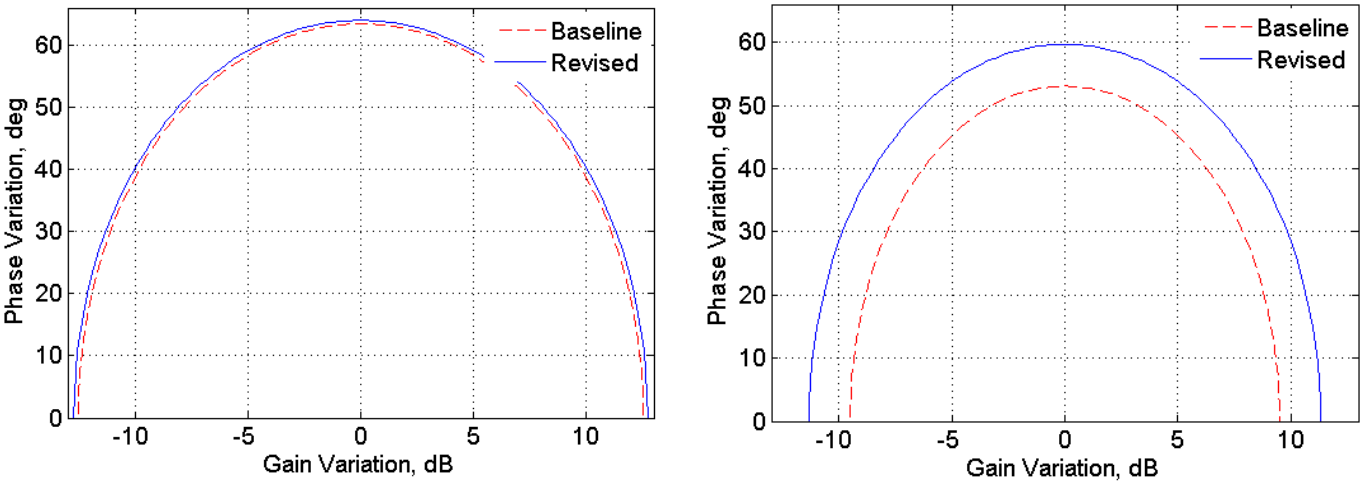

(a) Steady Maneuvers at $\phi = 60^o$

(b) Unsteady Maneuvers at $\phi = 60^o$

Figure 6. Disk Margin Analysis of the Baseline and Revised F/A-18 Flight Control Law

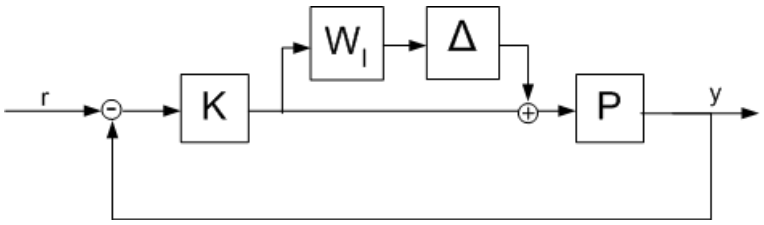

Figure 7. F/A-18 Input Multiplicative Uncertainty Structure

we introduce multiplicative uncertainty, $W_I \Delta_{IM}$, in all four input channels. The uncertainty Δ_{IM} represents unit norm bounded unmodeled dynamics. The weighting function will be set to unity for analysis purpose, $W_I = I_{4\times4}$. We will perform the structured-singular-value (μ) analysis. The $\frac{1}{\mu}$ value measures the stability margin due to the uncertainty description in the system.

1. Diagonal Input Multiplicative Uncertainty

Figure **??** shows the μ plot of both the closed loops at both steady and unsteady bank maneuvers, when the uncertainty, Δ_{IM}, has a diagonal structure. This models uncertainty in each actuation channel but no cross-coupling between the channels. The value of μ at each frequency ω is inversely related to the smallest uncertainty which causes the feedback system to have poles at $\pm j\omega$. Thus the largest value on the μ plot is equal to $1/k_m$ where k_m denotes the stability margin. In Figure **??**, the peak value of μ is 0.97 ($k_m = 1.03$) for both the revised and baseline controller during steady maneuvers, which indicates a very robust lfight control system. In addition, Figure **??** shows the peak value of μ for both the control laws at unsteady bank turn maneuvers. Here, the baseline flight controller exhibits a peak mu value of 1.25 ($k_m = 0.83$) and the revised flight controller achieves a μ value of 1.20 ($k_m = 0.80$). In both steady and unsteady maneuvers, both the controllers achieve similar stability margins for diagonal input multiplicative uncertainty across the input channel. These results corresponds well with the classical margin results in Section **??**.

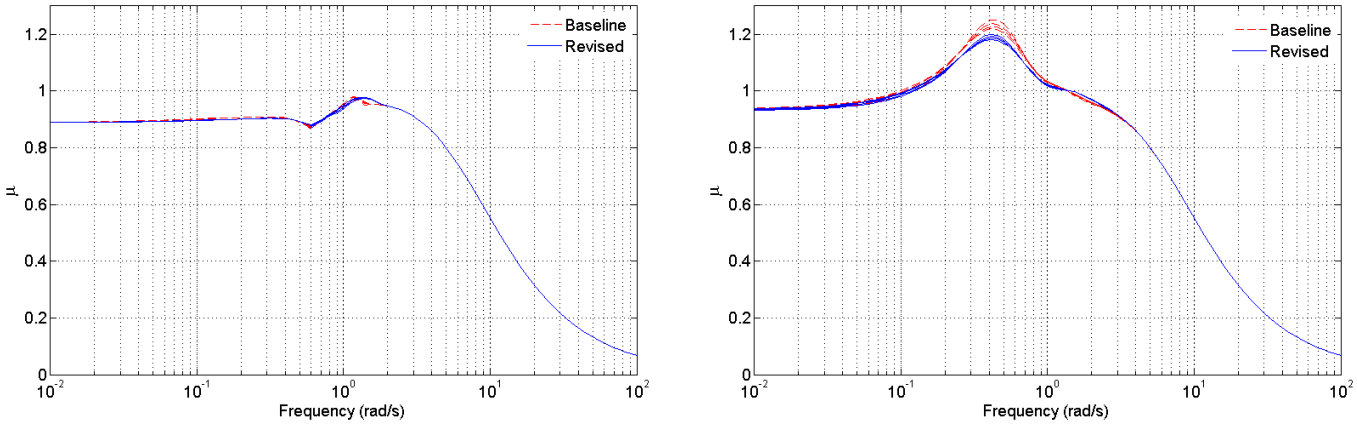

(a) Steady Maneuvers

(b) Unsteady Maneuvers

Figure 8. Diagonal Input Multiplicative Uncertainty Analysis of the Baseline and Revised F/A-18 Flight Control Law

2. Full Block Input Multiplicative Uncertainty

Figure **??** shows the μ plot(for both steady and unsteady maneuvers) when Δ_{IM} is allowed to be a full block uncertainty. This uncertainty structure models the effects of dynamic cross-coupling between the channels to determine how well the flight control laws are able to handle the coupling at the input to the F/A-18 actuators. As mentioned before, the falling leaf motion is an exaggerated form of in-phase Dutch-roll motion with large coupling in the roll-yaw direction. Increased robustness of the flight control law with respect to the full Δ_{IM} is associated with its ability to mitigate the onset of the falling leaf motion. Figure **??** shows the μ analysis for steady maneuvers. In this case, both the baseline and revised flight control law achieves similar stability margin ($\mu = 1.02$ and $k_m = 0.98$). Figure **??** shows the μ analysis for unsteady maneuvers. Here, the baseline flight controller exhibits a peak mu value of 1.25 ($k_m = 0.83$) and the revised flight controller achieves a μ value of 1.20 ($k_m = 0.80$). In both steady and unsteady maneuvers, both the controllers achieve similar stability margins for full input multiplicative uncertainty across the input channel.

Robustness analysis with respect to input multiplicative uncertainty (both full block and diagonal) across input channels has not detected any performance issue with the baseline flight control law compare to the revised flight control law. At this point, the linear analysis shows both controllers are very robust with similar stability margins and will mitigate the onset of the falling leaf motion.

D. Robustness Analysis to Parametric Uncertainty

So far we have provided a stability analysis with respect to unstructured dynamic uncertainty at the model inputs. Robustness analysis of flight control system with structured uncertainty is also important in validating closed-loop robustness and performance.[?] Moreover, robustness assessment of the flight control law due to the nonlinear variations of aerodynamic coefficients over the flight envelope needs to be considered. Including parametric uncertainty models into the analysis is one approach to address this issue. Both controllers are examined with respect to robustness in the presence of parametric variations in the plant model. To this end, we represented the stability derivatives of the linearized model with $\pm 10\%$ uncertainty around their nominal values. These terms are chosen carefully to represent the stability characteristics of theF/A-18 aircraft that play an important role in the falling leaf motion. These terms are related to the entries of the linearized open-loop A matrix. The terms in the lateral directions are: sideforce due to sideslip (Y_β); rolling moment due to sideslip (L_β); yawing moment due to sideslip (N_β); roll damping (L_p); yaw damping (N_r). The following longitudinal terms have also been considered: pitch damping (M_q): normal force due

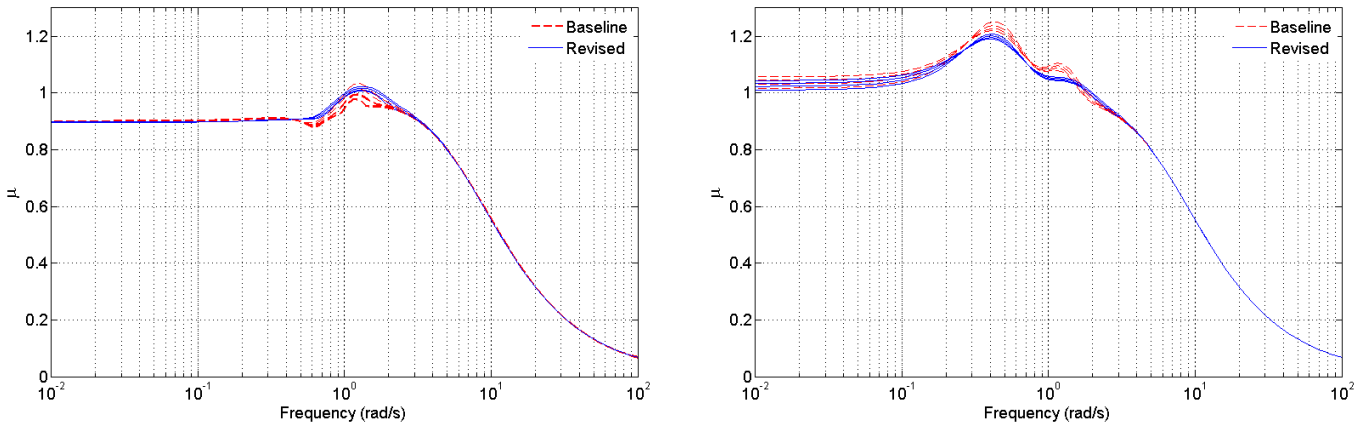

(a) Steady Maneuvers

(b) Unsteady Maneuvers

Figure 9. Full Block Input Multiplicative Uncertainty Analysis of the Baseline and Revised F/A-18 Flight Control Law

to pitch rate (Z_q); pitch stiffness (M_α). Cook[?] provides a detailed description of these terms. The lateral aerodynamic terms: Y_β, L_β, N_β, L_p, and N_r correspond respectively to the $(1,1)$, $(2,1)$, $(3,1)$, $(2,2)$, and $(3,3)$ entries of the linearized A matrix presented in previous section. The longitudinal aerodynamic terms: M_q, Z_q, and M_α correspond respectively to the $(6,6)$, $(5,6)$, and $(6,5)$ entries of the same linearized A matrix.

Figure **??** shows the μ plot (for both steady and unsteady maneuvers) of both closed-loop systems with respect to this parametric uncertainty. For steady maneuvers, in Figure **??**, the stability margin for parametric uncertainty in the aerodynamic coefficients of the revised controller ($\mu = 0.092$ and $k_m = 10.8$) is approximately 1.3 times larger than that of the baseline controller ($\mu = 0.115$ and $k_m = 8.7$). For unsteady maneuvers, in Figure **??**, the stability margin for parametric uncertainty in the aerodynamic coefficients of the revised controller ($\mu = 0.109$ and $k_m = 9.17$) is approximately 1.2 times larger than that of the baseline controller ($\mu = 0.131$ and $k_m = 7.63$). Hence, the revised flight controller is more robust to error in aerodynamic derivatives than the baseline design, but overall both are very robust designs.

To this point, the linear robustness analysis indicate both the revised and baseline flight control laws are slightly less robust for unsteady maneuvers compare to the steady maneuvers. However, both the control laws achieve similar robustness properties separately for steady and unsteady maneuvers. The linear robustness analysis for the F/A-18 flight control laws do not indicate any dramatic improvement in departure resistance for the revised flight control compare to the baseline flight control law. This is contrary to the fact that the revised flight control law has been tested to be more robust as it is able to suppress the falling leaf motion problem in the F/A-18 Hornet aircraft. Hence, this motivates us to investigate the nonlinear stability analysis for both the flight control laws.

E. Nonlinear Analysis

The linear analysis is a local analysis which is only valid near the operating point. Many systems, including the F/A-18 aircraft, are more accurately described by nonlinear dynamical systems. For linear systems asymptotic stability of an equilibrium point is a global property. In other words, if the equilibrium point is asymptotically stable then the state trajectory will converge back to the equilibrium when starting from any initial condition. A key difference with nonlinear systems is that equilibrium points may only be locally asymptotically stable. Khalil[?] and Vidyasagar[?] provide good introductory discussions of this issue. The region-of-attraction (ROA) of an asymptotically stable equilibrium point is the set of initial conditions whose

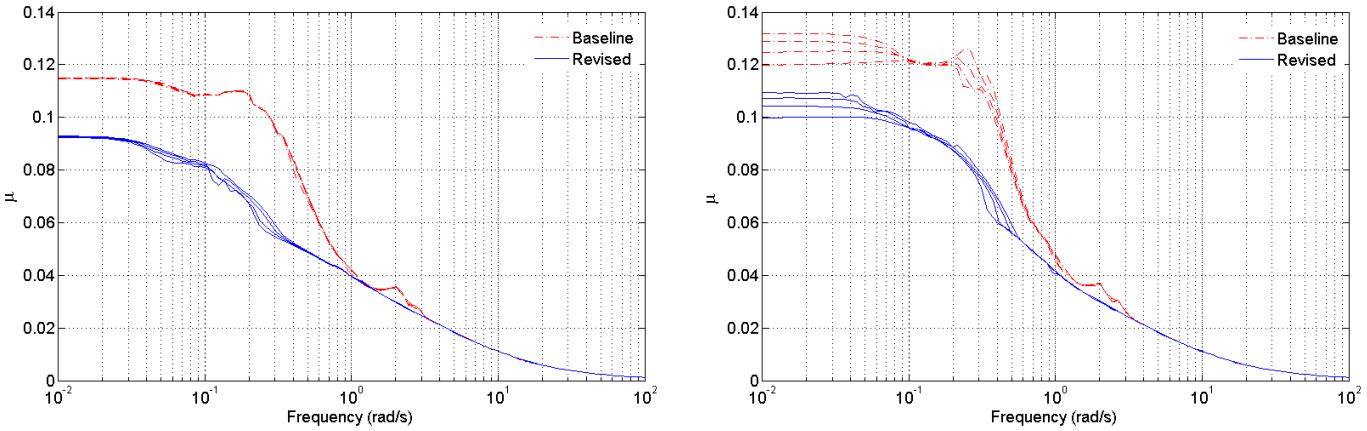

(a) Steady Maneuvers

(b) Unsteady Maneuvers

Figure 10. Stability Analysis of the Baseline and Revised F/A-18 Flight Control Law with Real Parametric Uncertainty in Aerodynamic Coefficients

state trajectories converge back to the equilibrium.[?] If the ROA is small, then a disturbance can easily drive the system out of the ROA and the system will then fail to come back to the stable equilibrium point. Thus the size of the ROA is a measure of the stability properties of a nonlinear system around an equilibrium point. This provides the motivation to estimate the region-of-attraction (ROA) for an equilibrium point of a nonlinear system. In this section we describe our technical approach to estimating the ROA and its application to estimate the ROA for the closed loop F/A-18 system with both the baseline and revised control laws.

1. Technical Approach

We consider autonomous nonlinear dynamical systems of the form:

$$\dot{x} = f(x),\ x(0) = x_0 \tag{1}$$

where $x \in \mathbb{R}^n$ is the state vector. We assume that $x = 0$ is a locally asymptotically stable equilibrium point. Formally, the ROA is defined as:

$$R_0 = \left\{ x_0 \in \mathbb{R}^n :\ \text{If } x(0) = x_0 \text{ then } \lim_{t\to\infty} x(t) = 0 \right\} \tag{2}$$

Computing the exact ROA for nonlinear dynamical systems is very difficult. There has been significant research devoted to estimating invariant subsets of the ROA.[?,?,?,?,?,?,?,?,?,?] Our approach is to restrict the search to ellipsoidal approximations of the ROA. The ellipsoid is specified by $\{x_0^T N x_0 \leq \beta\}$ where $N = N^T > 0$ is a user-specified matrix which determines the shape of the ellipsoid. Given N, the problem is to find the largest ellipsoid contained in the ROA:

$$\begin{aligned} \beta^* = &\max \beta \\ &\text{subject to: } \{x_0^T N x_0 \leq \beta\} \subset R_0 \end{aligned} \tag{3}$$

Determining the best ellipsoidal approximation to the ROA is still a challenging computational problem. Instead we will attempt to solve for upper and lower bounds satisfying $\underline{\beta} \leq \beta^* \leq \bar{\beta}$. If these upper and lower bounds are close then we have approximately solved the best ellipsoidal approximation problem given in Equation **??**.

The upper bounds are computed via a search for initial conditions leading to divergent trajectories. If $\lim_{t\to\infty} x(t) = +\infty$ when starting from $x(0) = x_{0,div}$ then $x_{0,div} \notin R_0$. If we define $\bar{\beta}_{div} := x_{0,div}^T N x_{0,div}$ then $\{x_0^T N x_0 \leq \bar{\beta}_{div}\} \not\subset R_0$. Thus $\bar{\beta}_{div}$ is a true upper bound on β^* and $\{x_0^T N x_0 \leq \bar{\beta}_{div}\}$ is an outer approximation of the best ellipsoidal approximation to the ROA. We use an exhaustive Monte Carlo search to find the tightest possible upper bound on β^*. Specifically, we randomly choose initial conditions starting on the boundary of a large ellipsoid: Choose x_0 satisfying $x_0^T N x_0 = g$ where g is sufficiently large that $g \gg \beta^*$. If a divergent trajectory is found, then the initial condition is stored and an upper bound on β^* is computed. g is then decreased by a factor of 0.995 and the search continues until a maximum number of simulations is reached. $\bar{\beta}_{MC}$ will denote the smallest upper bound computed with this Monte Carlo search.

The lower bounds are computed using Lyapunov functions and recent results connecting sums-of-squares polynomials to semidefinite programming. To compute these bounds we need to further assume that the vector field $f(x)$ in the system dynamics (Equation **??**) is a polynomial function. We briefly describe the computational algorithm here and full algorithmic details are provided elsewhere.[?,?,?,?,?,?,?] Lemma **??** is the main Lyapunov theorem used to compute lower bounds on β^*. This specific lemma is proved by Tan[?] but very similar results are given in textbooks, e.g. by Vidyasagar.[?]

Lemma 1 *If there exists a continuously differentiable function $V : \mathbb{R}^n \to \mathbb{R}$ such that:*

- $V(0) = 0$ *and* $V(x) > 0$ *for all* $x \neq 0$
- $\Omega_\gamma := \{x \in \mathbb{R}^n \ : \ V(x) \leq \gamma\}$ *is bounded.*
- $\Omega_\gamma \subset \{x \in \mathbb{R}^n \ : \ \nabla V(x) f(x) < 0\}$

then for all $x \in \Omega_\gamma$, the solution of Equation **??** *exists, satisfies $x(t) \in \Omega_\gamma$ for all $t \geq 0$, and $\Omega_\gamma \subset R_0$.*

A function V satisfying the conditions in Lemma **??** is a Lyapunov function and Ω_γ provides an estimate of the region of attraction. Any subset of Ω_γ is also inside the ROA. In principle we can compute a lower bound on β^* by solving the maximization:

$$\begin{aligned} \underline{\beta} := & \max \beta \\ & \text{subject to: } \{x_0^T N x_0 \leq \beta\} \subset \Omega_\gamma \end{aligned} \tag{4}$$

Our computational algorithm replaces the set containment constraint with a sufficient condition involving non-negative functions:

$$\begin{aligned} \underline{\beta} := & \max \beta \\ & \text{subject to: } s(x) \geq 0 \ \forall x \\ & \qquad -(\beta - x^T N x) s(x) + (\gamma - V(x)) \geq 0 \ \forall x \end{aligned} \tag{5}$$

The function $s(x)$ is a decision variable of the optimization, i.e. it will be found as part of the optimization. It is a "multiplier" function. It is straight-forward to show that the two non-negativity conditions in Optimization **??** are a sufficient condition for the set containment condition in Optimization **??**. If both $V(x)$ and $s(x)$ are restricted to be polynomials then both constraints involve the non-negativity of polynomial functions. A sufficient condition for a generic multi-variate polynomial $p(x)$ to be non-negative is the existence of polynomials $\{g_1, \ldots, g_n\}$ such that $p = g_1^2 + \cdots + g_n^2$. A polynomial which can be decomposed in this way is rather appropriately called a sum-of-squares (SOS). Finally, if we replace the non-negativity conditions in Optimization **??** with SOS constraints, then we arrive at an SOS optimization problem:

$$\begin{aligned} \underline{\beta} := & \max \beta \\ & \text{subject to: } s(x) \text{ is } SOS \\ & \qquad -(\beta - x^T N x) s(x) + (\gamma - V(x)) \text{ is } SOS \end{aligned} \tag{6}$$

It is sufficient to note that there are connections between SOS polynomials and semidefinite matrices. Moreover, optimization problems involving SOS constraints can be converted and solved as a semidefinite programming optimization. There is freely available software to set up and solve these problems.[?,?,?]

The choice of the Lyapunov function which satisfies the conditions of Lemma **??** has a significant impact on the quality of the lower bound,$\underline{\beta}$. The simplest method is to find $P > 0$ which solves the Lyapunov equation $A^T P + PA = -I$. $A := \left.\frac{\partial f}{\partial x}\right|_{x=0}$ is the linearization of the dynamics about the origin. $V_{LIN}(x) := x^T P x$ is a quadratic Lyapunov function since $x = 0$ is assumed to be a locally asymptotically stable equilibrium point. Thus we can solve for the largest value of γ satisfying the set containment condition in Lemma **??**: $\Omega_\gamma \subset \{x \in \mathbb{R}^n \ : \ \nabla V_{LIN}(x) f(x) < 0\}$. This problem can also be turned into an SOS optimization with "multiplier" functions as decision variables. $\underline{\beta}_{LIN}$ will denote the lower bound obtained using the quadratic Lyapunov function obtained from linearized analysis.

Unfortunately, $\underline{\beta}_{LIN}$ is typically orders of magnitude smaller than the upper bound $\bar{\beta}_{MC}$. Several methods to compute better Lyapunov functions exist, including V-s iterations,[?,?,?,?] bilinear optimization,[?] and use of simulation data.[?,?] We applied the V-s iteration starting from V_{LIN}. In the first step of the iteration, the multiplier functions and $\underline{\beta}_{LIN}$ are computed. Then the multiplier functions are held fixed and the Lyapunov function candidate becomes the decision variable. The SOS constraints of this new problem are those which arise from the two set containment conditions: $\Omega_\gamma \subset \{x \in \mathbb{R}^n \ : \ \nabla V_{LIN}(x) f(x) < 0\}$ and $\{x_0^T N x_0 \leq \beta\} \subset \Omega_\gamma$. In the next iteration, the multiplier functions are again decision variables and a lower bound is computed using the new Lyapunov function computed in the previous iteration. The V-s iteration continues as long as the lower bound continues to increase. In this iteration, we can allow Lyapunov functions of higher polynomial degree. Increasing the degree of the Lyapunov function will improve the lower bound at the expense of computational complexity. The computational time grows very rapidly with the degree of the Lyapunov function and so degree 4 candidates are about the maximum which can be used for problems like the F/A-18 analysis. $\underline{\beta}_2$ and $\underline{\beta}_4$ denote the best lower bounds computed with the V-s iteration for quadratic and quartic Lyapunov functions.

2. ROA Analysis for F/A-18

Computing the exact ROA for a dynamical system is challenging. In this paper, we will focus on estimating the lower bound of the ROA for the F/A-18 aircraft using the V-s iteration. Moreover, the ROA analysis is a local nonlinear analysis. In this section, we will estimate the lower bound of the ROA for the F/A-18 aircraft operating at a steady ($\beta \neq 0$) bank turn of $\phi = 60^o$. The ROA results presented in this section uses the cubic degree polynomial models for 60^o steady bank turn maneuver as described in Appendix **??**. The ordering of the state vector is $x^T := [\beta,\ \mathrm{p},\ \mathrm{r},\ \phi,\ \alpha,\ \mathrm{q},\ x_c]$. The shape matrix for the ellipsoid is chosen to be $N := (5^o)^2 \cdot diag(5^o, 20^o, 5^o, 45^o, 25^o, 25^o, 25^o)^{-2}$. This roughly scales each state by the maximum magnitude observed during flight conditions. The factor of $(5^o)^2$ normalizes the largest entry of the matrix N to be equal to one. The ellipsoid, $x^T N x = \underline{\beta}$, defines the lower bound of the ROA for the F/A-18 aircraft around the operating point. This estimated ROA ellipsoid for the F/A-18 aircraft defines the set of initial conditions which will bring the aircraft back to its trim point. In other words, the F/A-18 aircraft will be operating within a safe flight envelope even if the aircraft is perturbed from its operating point due to wind gusts, disturbances or any upset condition and still remains within the ROA ellipsoid. Hence, the ROA provides a measure of how much perturbation the aircraft can tolerate before it becomes unstable. This measure is given the value of the $\underline{\beta}$. Hence, the value of the $\underline{\beta}$ can be thought of as 'nonlinear stability margin', similar to the linear stability margin (k_m) concept presented in Section **??**. However, these two margins are not comparable to each other. Now, we will present the results on the lower bound estimate of the ROA for both baseline and revised control law.

As previously mentioned, increasing the degree of the Lyapunov function will improve the lower bound estimate of the ROA. In this paper, we will use linearized, quadratic, and quartic Lyapunov functions to estimate the lower bound on the ROA. Current practice in validating flight control law involve estimating the ROA using the linearized Lyapunov function. Linearized Lyapunov function results in a very conservative estimate of the lower bound of the ROA. For the lower bounds, we computed $\underline{\beta}_{LIN} = 8.05 \times 10^{-5}$ for the baseline control law and $\underline{\beta}_{LIN} = 1.91 \times 10^{-4}$ for the revised control law. These lower bounds are not particularly useful since they are two to three orders of magnitude smaller than the corresponding upper bounds computed via Monte Carlo search, as mentioned in Section **??**. The lower bounds computed with the V-s iteration are significantly better. The V-s iteration with quadratic Lyapunov functions gives $\underline{\beta}_2 = 3.45 \times 10^{-3}$ for the baseline control law and $\underline{\beta}_2 = 9.43 \times 10^{-3}$ for the revised control law. The V-s iteration with quartic Lyapunov functions is even larger: $\underline{\beta}_4 = 1.24 \times 10^{-2}$ for the baseline control law and $\underline{\beta}_4 = 2.53 \times 10^{-2}$ for the revised control law. Figure **??** shows a comparison of the ROA estimate between the

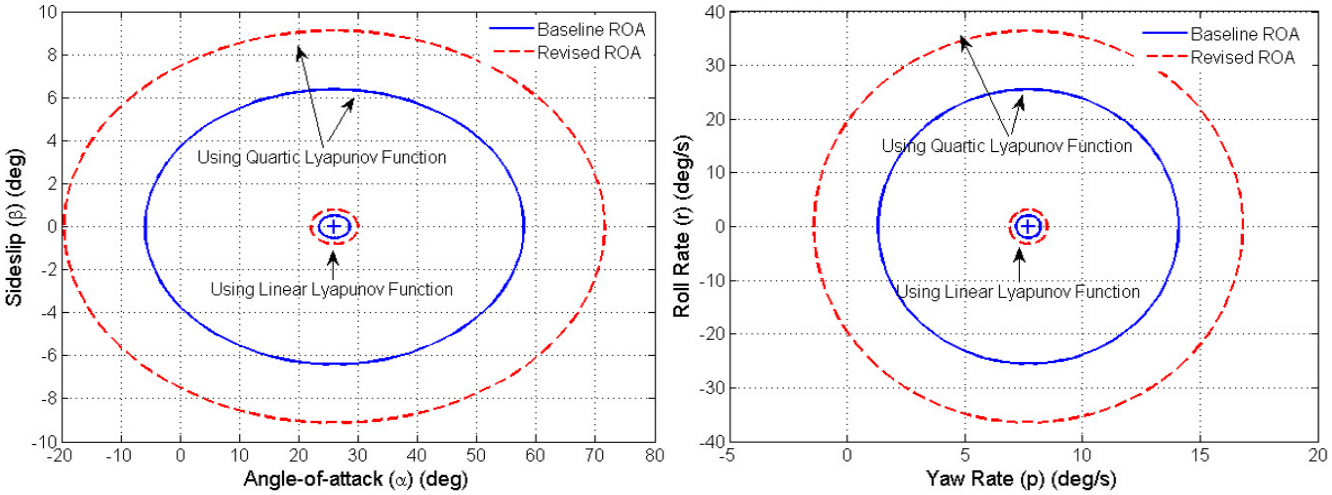

(a) ROA Estimation in $\alpha - \beta$ Space

(b) ROA Estimation in p − r Space

Figure 11. Region-of-Attraction Estimation with both Linearized and Quartic Lyapunov Function

linearized and quartic Lyapunov function in the $\alpha - \beta$ and p − r state space. The dashed ellipsoid represents the invariant sets for the revised flight control law whereas the solid represents the baseline flight control law. Currently in the industry, flight control laws are validated against the ROA estimate based on the linearized Lyapunov function. However, the linearized analysis is very conservative compare to the analysis based on the quartic ($\partial V = 4$) Lyapunov function.

The estimated lower bound of the ROA defines a guaranteed stability region for the F/A-18 aircraft. However, this is not an exact value of the lower bound. This motivates us to estimate the upper bound of the ROA. The upper bound estimation is done via Monte Carlo search for unstable trajectories as mentioned in Section **??**. The results are presented in the following section.

3. Monte Carlo Analysis for F/A-18

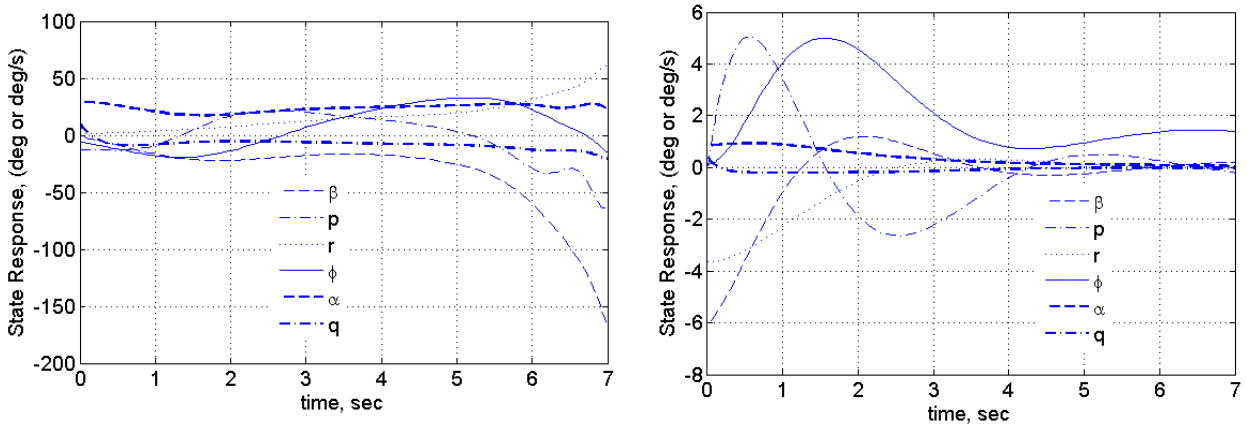

(a) Unstable Trajectory with Initial Condition s.t. $||x_0^T N x_0||_2 = 0.0155$

(b) Stable Trajectory with Initial Condition s.t. $||x_0^T N x_0||_2 = 0.0154$

Figure 12. Time Response of F/A-18 Aircraft Baseline Closed Loop Model

For estimating the upper bounds, we performed the Monte Carlo search with a maximum of 2 million simulations each for the baseline and revised control laws. The baseline control law provides an upper bound of $\bar{\beta}_{MC} = 1.56 \times 10^{-2}$ whereas the revised control law provides an upper bound of $\bar{\beta}_{MC} = 2.95 \times 10^{-2}$. This means that an initial condition has been found on the boundary of the ellipsoid, defined by $||x_0^T N x_0||_2 = \bar{\beta}_{MC}$, causing the system to go unstable. Hence, the value of the $\bar{\beta}_{MC}$ provides a measure of the upper bound of the ROA for the F/A-18 aircraft.

Figure **??** shows the unstable response of the baseline system resulting from an initial condition , $x^T := [-1.1206^o,\ -12.3353^o,\ 1.5461^o,\ -5.8150^o,\ 28.9786^o,\ 9.9211^o,\ 0]$, chosen randomly from an ellipsoid of size 0.0156 ($||x_0^T N x_0||_2 = 0.0155$). Figure **??** shows a stable trajectory of the baseline system where the initial condition is chosen from an ellipsoid approximately a factor of 0.995 ($||x_0^T N x_0||_2 = 0.0154$) smaller than the unstable one. This initial condition for the stable trajectory is: $x^T := [-6.1235^o,\ -0.0923^o, 3.6486^o,\ 0.1241^o,\ 0.8388^o,\ 0.4142$

Similarly, Figure **??** shows instability in the revised system. The initial condition (in degree) for the unstable trajectory, $x^T := [0.3276^o,\ -8.0852^o,\ 2.8876^o,\ -2.1386^o,\ 44.8282^o,\ 9.9829^o,\ 0]$, chosen randomly from an ellipsoid of size 0.0295 ($||x_0^T N x_0||_2 = 0.0295$). Figure **??** shows a stable trajectory of the revised system where the initial condition is chosen from an ellipsoid approximately a factor of 0.995 (($||x_0^T N x_0||_2 = 0.0294$) smaller than the unstable one. This initial condition for the stable trajectory is, $x^T := [-9.2591^o,\ 4.0494^o, 1.8494^o,\ 11.2362^o,\ 10.6863^o,\ 1.1840^o,\ 0]$.

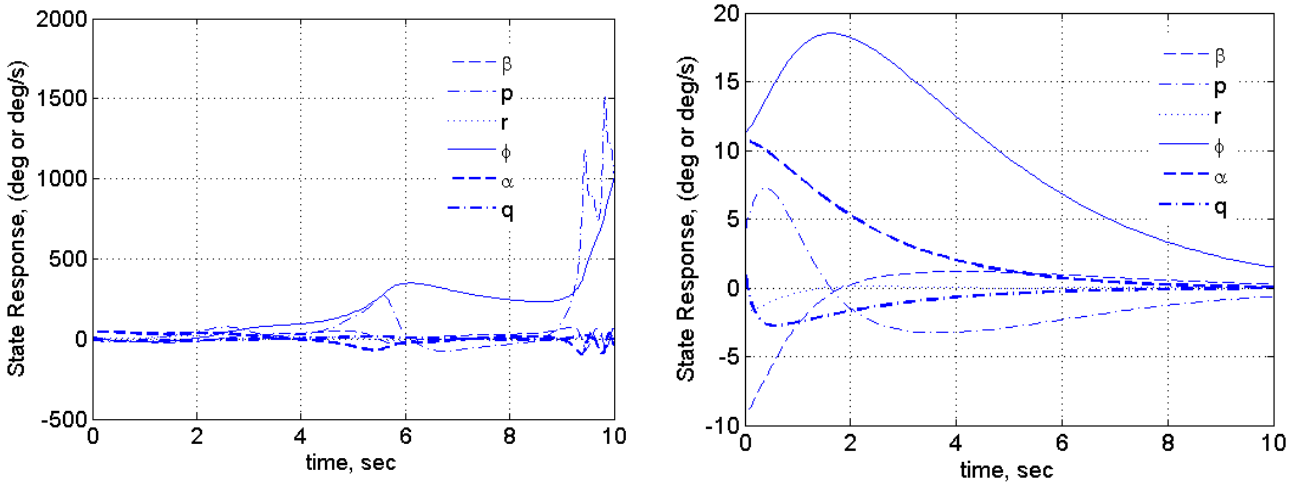

(a) Unstable Trajectory with Initial Condition s.t. $||x_0^T N x_0||_2 = 0.0295$ (b) Stable Trajectory with Initial Condition s.t. $||x_0^T N x_0||_2 = 0.0294$

Figure 13. Time Response of F/A-18 Aircraft Revised Closed Loop Model

To this point, we have computed the lower and upper bounds on β^* as described in Section **??**. The results on both these bounds are presented above. The provable invariant region (lower bound of the ROA) for the $\alpha - \beta$ state is given by the solid ellipses in Figure **??**. Any initial condition of α, and β states (while other states are at equilibrium) inside the solid region will converge back to the trim point (marked as '+'). The dashed ellipses in the Figure **??** provides an upper estimate of the ROA boundary on which an initial condition has been found that causes instability. Similarly, the solid ellipses in Figure **??** plots the provable invariant region in the the roll rate(p) - yaw rate(r) direction for both the control laws. Again, the dashed ellipses represent the upper bound of the ROA estimate computed via Monte Carlo search.

The local nonlinear ROA analysis has established two important facts: (i) For the baseline flight control law, the bound on the invariant sublevel sets of the ROA is: $1.24 \times 10^{-2} \leq \beta* \leq 1.56 \times 10^{-2}$, and (ii) For the revised flight control law, the bound on the invariant sublevel sets of the ROA is : $2.53 \times 10^{-2} \leq \beta* \leq 2.95 \times 10^{-2}$.

As mentioned before, size of the ROA (value of $\beta*$) indicates the 'nonlinear stability margin' of the system. The revised flight control law achieves a factor of $\sqrt{\frac{2.53\times10^{-2}}{1.24\times10^{-2}}} = 1.43$ larger guaranteed stability region in each state space direction compare to the baseline flight control law. Overall, the revised flight control law has a factor of $1.43^7 = 12.22$ RECHECK Not Right larger volume than the

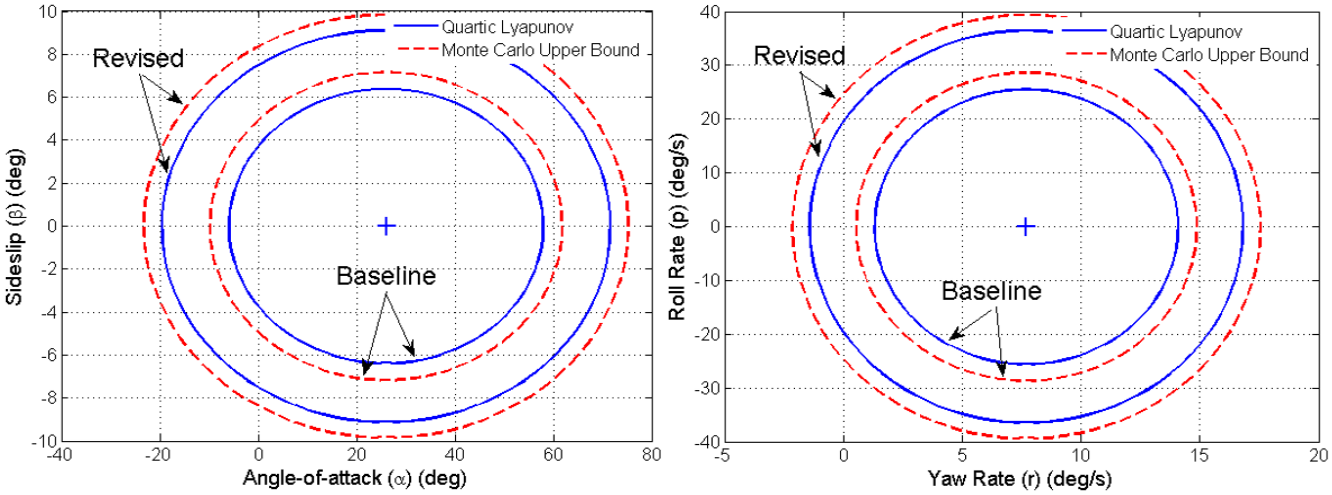

(a) Estimation of α-β Region-of-Attraction

(b) Estimation of p -r Region-of-Attraction

Figure 14. Lower and Upper Bound Estimate of ROA for Baseline and Revised Flight Control Law around Steady 60^o Bank Turn

baseline flight control law. This indicates that the revised flight control law is more likely to suppress the onset of the falling leaf motion compare to the baseline control law.

The ROA results based on the quartic Lyapunov function in Figure **??** proves that the baseline flight control law can tolerate a perturbation of $\approx \pm 30^o$ in α direction while the revised flight control law can tolerate a perturbation of $\approx \pm 45^o$. Similarly, the revised flight control law also achieves a larger ROA compare to the baseline flight control law in the roll rate(p) - yaw rate(r) direction.

VI. Summary

Table **??** shows a summary of all of the stability analysis results described in this section. The analysis results are based on the linear plant for 60^o steady bank angle turn (provided in Appendix C).

Table 6. Summary of Analysis Results

Linear Analysis	Baseline	Revised
Multivariable Loop Phase Margin	$\pm 63.4°$	$\pm 64.0°$
Multivariable Loop Gain Margin (dB)	± 12.53	± 12.73
Diagonal Input Multiplicative: $(k_m = \frac{1}{\mu})$	1.03	1.03
Full Input Multiplicative: $(k_m = \frac{1}{\mu})$	0.98	0.98
Parametric Uncertainty: $(k_m = \frac{1}{\mu})$	8.70	10.8
Nonlinear Analysis: $\{x^{\mathrm{T}} N x \leq \beta^*\}$		
Linearized Lyapunov Function, $\underline{\beta}_{lin}$	8.05×10^{-5}	1.91×10^{-4}
Generic Quadratic Lyapunov Function, $\underline{\beta}_2$	3.45×10^{-3}	9.43×10^{-3}
Generic Quartic Lyapunov Function, $\underline{\beta}_4$	1.24×10^{-2}	2.53×10^{-2}
Monte Carlo Simulation, $\bar{\beta}_{MC}$	1.56×10^{-2}	2.95×10^{-2}

The out-of-control falling leaf motion in the F/A-18 aircraft has been mitigated by modifying the baseline flight control law. We have employed both linear and nonlinear analysis to compare the stability margins between the baseline and revised flight control law. The linear robustness analysis did not detect any stability issues with either of the control laws. More importantly, the linear analysis established similar

stability margin (k_m) for both the control laws, as seen in Table **??**. This is contrary to the fact that the revised flight control law has been tested to prove its ability to suppress the falling leaf motion. However, the nonlinear ROA analysis shows a dramatic improvement in the stability region for the revised flight control law compare to the baseline flight control law. Enlargement of the stability region indicates that the revised flight control law can tolerate more perturbation and able to suppress the falling leaf motion.

VII. Conclusion

In this paper, we have compared the stability and robustness properties of the two control laws (the baseline and the revised) of the F/A-18 aircraft using linear robustness concepts and nonlinear region-of-attraction analysis tools. The nonlinear ROA analysis showed that the revised control law has better robustness properties compare to the baseline control law, whereas the linear analysis showed similar stability margins for both the control laws. Sum-of-Squares programming has been used to establish guaranteed stability region for the nonlinear F/A-18 aircraft models. This is the first time that this technique has been successfully applied to a real physical system. This approach provides a guaranteed stability certificate for the control law as oppose to the widely used exhaustive Monte Carlo simulation technique.

Acknowledgments

This research was supported under a NASA Langley NRA NNH077ZEA001N entitled "Analytical Validation Tools for Safety Critical Systems." The technical contract monitor was Dr. Christine Belcastro. We would also like to thank Dr. Ufuk Topcu at Caltech and Prof. Andrew Packard at University of California at Berkley for useful discussions.

Appendix

A. Full Model

Here we present the full six degree-of-freedom F/A-18 Hornet model. Again, this model is not directly used for analysis presented in this paper. This model is provided for completeness. We will provide both the equations of motion and the aerodynamic model.

1. Equations of Motion

The equations of motion described here have been taken from the report (chapter 4) by Napolitano and Spagnuolo.[?] The equations of motion presented here will be in terms of the following state variables:

$$\mathbf{X}^{\mathrm{T}} = [V_{TAS} \quad \alpha \quad \beta \quad p \quad q \quad r \quad \phi \quad \theta \quad \psi]$$

The following three equations describe the force equations of the aircraft:

$$\begin{aligned}\dot{V_T} = &-\frac{\bar{q}S}{m}(C_D\cos\beta - C_Y\sin\beta) + g(\cos\phi\cos\theta\sin\alpha\cos\beta + \sin\phi\cos\theta\sin\beta \\ &- \sin\theta\cos\alpha\cos\beta) + \frac{T}{m}\cos\alpha\cos\beta\end{aligned}$$

$$\begin{aligned}\dot{\alpha} = &-\frac{\bar{q}S}{mV_T\cos\beta}C_L + \mathrm{q} - \tan\beta(\mathrm{p}\cos\alpha + r\sin\alpha) \\ &+ \frac{g}{V_T\cos\beta}(\cos\phi\cos\theta\cos\alpha + \sin\alpha\sin\theta) - \frac{T\sin\alpha}{mV_T\cos\beta}\end{aligned}$$

$$\begin{aligned}\dot{\beta} = &\frac{\bar{q}S}{mV_T}(C_Y\cos\beta + C_D\sin\beta) + \mathrm{p}\sin\alpha - \mathrm{r}\cos\alpha + \frac{g}{V_T}\cos\beta\sin\phi\cos\theta \\ &+ \frac{\sin\beta}{V_T}(g\cos\alpha\sin\theta - g\sin\alpha\cos\phi\cos\theta + \frac{T}{m}\cos\alpha)\end{aligned}$$

The following equation describes the moment equations of the aircraft:

$$\begin{aligned}
\dot{\mathrm{p}} &= \frac{1}{\kappa}(I_{zz}L + I_{xz}N - [I_{xz}(I_{yy} - I_{xx} - I_{zz})]\mathrm{pq} - [I_{xz}^2 + I_{zz}(I_{zz} - I_{yy})]\mathrm{rq}) \\
\dot{\mathrm{q}} &= \frac{1}{I_{yy}}(M - I_{xz}(\mathrm{p}^2 - \mathrm{r}^2) + (I_{zz} - I_{xx})\mathrm{pr}) \\
\dot{\mathrm{r}} &= \frac{1}{\kappa}(I_{xz}L + I_{xx}N + [I_{xz}(I_{yy} - I_{xx} - I_{zz})]\mathrm{rq} + [I_{xz}^2 + I_{xx}(I_{xx} - I_{yy})]\mathrm{pq})
\end{aligned}$$

where $\kappa = I_{xx}I_{zz} - I_{xz}^2$ and L, M, N indicates roll, pitch, and yaw moment:

$$\begin{bmatrix} L \\ M \\ N \end{bmatrix} = \begin{bmatrix} C_l \bar{q} S b \\ C_m \bar{q} S \bar{c} \\ C_n \bar{q} S b \end{bmatrix}$$

The following equation provides the kinematic relations of the aircraft:

$$\begin{Bmatrix} \dot{\phi} \\ \dot{\theta} \\ \dot{\psi} \end{Bmatrix} = \begin{bmatrix} 1 & \sin\phi\tan\theta & \cos\phi\tan\theta \\ 0 & \cos\phi & -\sin\phi \\ 0 & \sin\phi\sec\theta & \cos\phi\sec\theta \end{bmatrix} \begin{Bmatrix} \mathrm{p} \\ \mathrm{q} \\ \mathrm{r} \end{Bmatrix}$$

2. Full Aerodynamic Model

The aerodynamic coefficients presented here have been extracted from various papers.[?,?,?,?] The aerodynamic model of the aircraft is presented below and the values have been given in Table **??**, **??**, and **??**.

$$\begin{aligned}
\text{Pitching Moment, } C_m &= C_{m_\alpha}\alpha + C_{m_0} + (C_{m_{\delta_{stab}}}\alpha + C_{m_{\delta_{stab_0}}})\delta_{stab} \\
&\quad + \frac{\bar{c}}{2V_T}(C_{m_q}\alpha + C_{m_{q_0}})\mathrm{q}
\end{aligned}$$

$$\begin{aligned}
\text{Rolling Moment, } C_l &= (C_{l_{\beta_2}}\alpha^2 + C_{l_{\beta_1}}\alpha + C_{l_{\beta_0}})\beta + (C_{l_{\delta_{ail}}}\alpha + C_{l_{\delta_{ail_0}}})\delta_{ail} \\
&\quad + (C_{l_{\delta_{rud}}}\alpha + C_{l_{\delta_{rud_0}}})\delta_{rud} + \frac{b}{2V_T}(C_{l_p}\alpha + C_{l_{p_0}})\mathrm{r}
\end{aligned}$$

$$\begin{aligned}
\text{Yawing Moment, } C_n &= (C_{n_{\beta_2}}\alpha^2 + C_{n_{\beta_1}}\alpha + C_{n_{\beta_0}})\beta + (C_{n_{\delta_{ail}}}\alpha + C_{n_{\delta_{ail_0}}})\delta_{ail} \\
&\quad + (C_{n_{\delta_{rud}}}\alpha + C_{n_{\delta_{rud_0}}})\delta_{rud} + (C_{n_r}\alpha + C_{n_{r_0}})\frac{b}{2V_T}\mathrm{r}
\end{aligned}$$

Table 7. Aerodynamic Moment Coefficients

Pitching Moment			Rolling Moment			Yawing Moment		
C_{m_α}	=	-0.9931	$C_{l_{\beta_2}}$	=	0.8102	$C_{n_{\beta_2}}$	=	-0.3917
C_{m_0}	=	0.1407	$C_{l_{\beta_1}}$	=	-0.6446	$C_{n_{\beta_1}}$	=	0.3648
$C_{m_{\delta_{stab}}}$	=	0.6401	$C_{l_{\beta_0}}$	=	-0.0427	$C_{n_{\beta_0}}$	=	0.0894
$C_{m_{\delta_{stab_0}}}$	=	-1.1055	$C_{l_{\delta_{ail}}}$	=	-0.1553	$C_{n_{\delta_{ail}}}$	=	-0.0213
C_{m_q}	=	-14.30	$C_{l_{\delta_{ail_0}}}$	=	0.1542	$C_{n_{\delta_{ail_0}}}$	=	0.0051
$C_{m_{q_0}}$	=	- 2.00	$C_{l_{\delta_{rud}}}$	=	-0.0858	$C_{n_{\delta_{rud}}}$	=	0.0534
			$C_{l_{\delta_{rud_0}}}$	=	0.0943	$C_{n_{\delta_{rud_0}}}$	=	-0.0724
			C_{l_p}	=	0.0201	C_{n_r}	=	-0.0716
			$C_{l_{p_0}}$	=	-0.3370	$C_{n_{r_0}}$	=	-0.4375

$$\text{Sideforce Coeffificent, } C_Y = (C_{Y_{\beta_2}}\alpha^2 + C_{Y_{\beta_1}}\alpha + C_{Y_{\beta_0}})\beta + (C_{Y_{\delta_{ail}}}\alpha + C_{Y_{\delta_{ail_0}}})\delta_{ail} + (C_{Y_{\delta_{rud}}}\alpha + C_{Y_{\delta_{rud_0}}})\delta_{rud}$$

$$\text{Lift Coefficient, } C_L = (C_{L_{\alpha_3}}\alpha^3 + C_{L_{\alpha_2}}\alpha^2 + C_{L_{\alpha_1}}\alpha + C_{L_{\alpha_0}})\cos(\frac{2\beta}{3}) (C_{L_{\delta_{stab}}}\alpha + C_{L_{\delta_{stab_0}}})\delta_{stab}$$

$$\text{Drag Coefficient, } C_D = (C_{D_{\alpha_4}}\alpha^4 + C_{D_{\alpha_3}}\alpha^3 + C_{D_{\alpha_2}}\alpha^2 + C_{D_{\alpha_1}}\alpha + C_{D_{\alpha_0}})\cos\beta + C_{D_0} + (C_{D_{\delta_{stab}}}\alpha + C_{D_{\delta_{stab_0}}})\delta_{stab}$$

Table 8. Aerodynamic Force Coefficients

Sideforce Coefficient			Drag Force Coefficient			Lift Force Coefficient		
$C_{Y_{\beta_2}}$	=	0.5781	$C_{D_{\alpha_4}}$	=	1.4610	$C_{L_{\alpha_3}}$	=	1.1645
$C_{Y_{\beta_1}}$	=	0.2834	$C_{D_{\alpha_3}}$	=	-5.7341	$C_{L_{\alpha_2}}$	=	-5.4246
$C_{Y_{\beta_0}}$	=	-0.8615	$C_{D_{\alpha_2}}$	=	6.3971	$C_{L_{\alpha_1}}$	=	5.6770
$C_{Y_{\delta_{rud}}}$	=	-0.4486	$C_{D_{\alpha_1}}$	=	-0.1995	$C_{L_{\alpha_0}}$	=	-0.0204
$C_{Y_{\delta_{rud_0}}}$	=	0.3079	$C_{D_{\alpha_0}}$	=	-1.4994	$C_{L_{\delta_{stab}}}$	=	-0.3573
$C_{Y_{\delta_{ail}}}$	=	0.4270	C_{D_0}	=	1.5036	$C_{L_{\delta_{stab_0}}}$	=	0.8564
$C_{Y_{\delta_{ail_0}}}$	=	-0.1047	$C_{D_{\delta_{stab}}}$	=	0.7771			
			$C_{D_{\delta_{stab_0}}}$	=	-0.0276			

B. Reduced Model

1. *Reduced Equations of Motion*

As mentioned before, we focus on the roll-coupled maneuvers of the aircraft for analysis. The reduced equations of motion emphasizing roll-coupled maneuvers[?] are presented in this section. The velocity, V_{TAS} has been assumed constant here, and equal to 250 ft/s.

$$\dot{\alpha} = -\frac{\bar{q}S}{mV_{TAS}}C_L + \mathrm{q} - \mathrm{p}\beta + \frac{g}{V_{TAS}} - \mathrm{r}\beta\alpha$$
$$\dot{\beta} = \frac{\bar{q}S}{mV_{TAS}}(C_D + C_Y\beta) + \mathrm{p}\alpha - \mathrm{r} + \frac{g}{V_{TAS}}\phi$$
$$\dot{\mathrm{p}} = \frac{1}{\kappa}(I_{zz}L + I_{xz}N - [I_{xz}^2 + I_{zz}(I_{zz} - I_{yy})]\mathrm{rq})$$
$$\dot{\mathrm{q}} = \frac{1}{I_{yy}}(M + (I_{zz} - I_{xx})\mathrm{pr})$$
$$\dot{\mathrm{r}} = \frac{1}{\kappa}(I_{xz}L + I_{xx}N + [I_{xz}^2 + I_{xx}(I_{xx} - I_{yy})]\mathrm{pq}$$
$$\dot{\phi} = \mathrm{p}$$

2. Reduced Aerodynamic Model

The rolling moment (C_l), pitching moment (C_m), yawing moment (C_n), and sideforce (C_Y) coefficients for the full aerodynamic model presented in Appendix A.2 are same for the reduced aerodynamic model. The lift and drag coefficients have been approximated by employing the standard least square approximation technique within $-20^\circ \leq \beta \leq 20^\circ$, and $-10^\circ \leq \alpha \leq 40^\circ$. The model is presented below:

Lift Coefficient, $C_L := C_{L_{\alpha_2}}\alpha^2 + C_{L_{\alpha_1}}\alpha + C_{L_{\alpha_0}} + (C_{L_{\delta_{stab}}}\alpha + C_{L_{\delta_{stab_0}}})\delta_{stab}$

Drag Coefficient, $C_D := C_{D_{\alpha_2}}\alpha^2 + C_{D_{\alpha_1}}\alpha + C_{D_{\beta_2}}\beta^2 + (C_{D_{\delta_{stab}}}\alpha + C_{D_{\delta_{stab_0}}})\delta_{stab}$

Table 9. Approximated Lift & Drag Force Coefficients

Drag Coefficient			Lift Coefficient		
$C_{D_{\alpha_2}}$	=	2.7663	$C_{L_{\alpha_2}}$	=	−4.5022
$C_{D_{\alpha_1}}$	=	0.1140	$C_{L_{\alpha_1}}$	=	5.4854
$C_{D_{\beta_2}}$	=	1.2838	$C_{L_{\alpha_0}}$	=	−0.0406
$C_{D_{\delta_{stab}}}$	=	0.7771	$C_{L_{\delta_{stab}}}$	=	−0.3573
$C_{D_{\delta_{stab_0}}}$	=	−0.0275	$C_{L_{\delta_{stab_0}}}$	=	0.8563

C. Linearized Model

The reduced order model presented in the Appendix B has been used to generate the linearized model. The linearization has been done around a trim point. The trim values for the states and the inputs are presented below. The model $x\dot{_{OL}} = Ax_{OL} + Bu$ with the output equation $y = Cx_{OL} + Du$ is presented in this section. The ordering of the states, inputs and outputs are mentioned below:

$$x_{OL}^{\mathrm{T}} = [\beta \quad p \quad r \quad \phi \quad \alpha \quad q \quad] \tag{7}$$
$$u = [\delta_{ail} \quad \delta_{rud} \quad \delta_{stab} \quad T] \tag{8}$$

However, the C and D matrices will be different for each of the control law.

$$y_{Baseline}^{\mathrm{T}} = [a_y \quad p \quad r \quad \alpha \quad q] \tag{9}$$
$$y_{Revised}^{\mathrm{T}} = [a_y \quad p \quad r \quad \alpha \quad \beta \quad q \quad \dot{\beta}] \tag{10}$$

The open loop plant, G , is represented as: $G = \left[\begin{array}{c|c} A & B \\ \hline C_{Revised} & D_{Revised} \end{array}\right]$ The linearized matrices for 60^o bank angle turn (Plant 4 in Table **??**) is presented here. The C and D matrices will be presented for the revised flight control law. Appropriate C and D matrices for the baseline flight control law can be extracted from the given matrices.

$$\left[\begin{array}{c|c} A & B \end{array}\right] = \left[\begin{array}{cccccc|cccc} -0.0059 & 0.4538 & -1 & 0.1288 & 0.0025 & 0 & 0.0046 & 0.0054 & 0 & 0 \\ -3.6680 & -0.4000 & 0.0134 & 0 & -0.0015 & -0.1095 & 1.8210 & 0.2573 & 0 & 0 \\ 0.1382 & 0.0070 & -0.1034 & 0 & -0.0184 & 0 & -0.0453 & -0.1459 & 0 & 0 \\ 0 & 1 & 0 & 0 & 0 & 0 & 0 & 0 & 0 & 0 \\ -0.0609 & 0 & 0 & 0 & -0.2201 & 1 & 0 & 0 & -0.0358 & -1.755 \times 10^{-6} \\ 0 & 0.1305 & 0 & 0 & -1.2550 & -0.1984 & 0 & 0 & -0.8269 & 0 \end{array}\right]$$

The C and D matrices for the revised controller are as follows:

$$\left[\begin{array}{c|c} C_{Revised} & D_{Revised} \end{array}\right] = \left[\begin{array}{cccccc|cccc} -0.2456 & 0 & 0 & 0 & 0.02005 & 0 & -0.04190 & 0.1232 & 0 & 0 \\ 0 & 1 & 0 & 0 & 0 & 0 & 0 & 0 & 0 & 0 \\ 0 & 0 & 1 & 0 & 0 & 0 & 0 & 0 & 0 & 0 \\ 0 & 0 & 0 & 0 & 1 & 0 & 0 & 0 & 0 & 0 \\ 0 & 0 & 0 & 0 & 0 & 1 & 0 & 0 & 0 & 0 \\ 0 & 0.4538 & -1 & 0.1288 & 0 & 0 & 0 & 0 & 0 & 0 \end{array}\right]$$

D. Control Law State Space Realization

The state space realization of both the baseline and the revised control laws will be presented here. The inputs to the controller will be the outputs (y) from the open-loop plant described in the previous section. The actuators have been set to unity ($= 1$) for analysis. The controller output can be denoted as the input (u) to the open-loop plant. The ordering of the controller input (y) and controller output (u) are same as described in the previous section. The controller state-space can be described as:

$$\dot{x}_c = A_c x_c + B_c y \tag{11}$$

$$u = C_c x_c + D_c y \tag{12}$$

The controller, $K = \left[\begin{array}{c|c} A_c & B_c \\ \hline C_c & D_C \end{array}\right]$ is in negative feedback with the open loop plant, G, described in the previous section. The closed-loop model, P_c, can be represented using the Matlab notation: $P_c = \text{feedback}(G, K)$.

1. *Baseline Controller Realization*

The baseline controller is presented below. Here, $y = y_{Baseline}$.

$$\left[\begin{array}{c|c} A_c & B_c \\ \hline C_c & D_c \end{array}\right] = \left[\begin{array}{c|ccccc} -1 & 0 & 0 & 4.9 & 0 & 0 \\ \hline 0 & 0 & 0.8 & 0 & 0 & 0 \\ -1 & -0.5 & 0 & -1.1 & 0 & 0 \\ 0 & 0 & 0 & 0 & -0.8 & -8 \\ 0 & 0 & 0 & 0 & 0 & 0 \end{array}\right]$$

2. *Revised Controller Realization*

The state-space realization of the revised controller has been presented below. Here, $y = y_{Revised}$.

$$\left[\begin{array}{c|c} A_c & B_c \\ \hline C_c & D_c \end{array}\right] = \left[\begin{array}{c|ccccccc} -1 & 0 & 0 & 4.9 & 0 & 0 & 0 & 0 \\ \hline 0 & 0 & 0.8 & 0 & 0 & 2 & 0 & 0.5 \\ -1 & -0.5 & 0 & -1.1 & 0 & 0 & 0 & 0 \\ 0 & 0 & 0 & 0 & -0.8 & 0 & -8 & 0 \\ 0 & 0 & 0 & 0 & 0 & 0 & 0 & 0 \end{array}\right]$$

E. 3^{rd} Order Approximated Polynomial Closed-Loop Models

We have presented the reduced order model and the aerodynamic coefficients, in Appendix **??**, necessary to build up the approximated polynomial F/A-18 model. The negative feedback of the controller with the nonlinear polynomial plant results in a rational closed-loop model. Least squares has been used to generate the 3^{rd} order polynomial models. Both the baseline and revised closed loop models have been presented below. These models have been used for the analysis presented in Section **??** and Section 3.0.1.

1. Baseline Closed Loop Model

$$\begin{aligned}\dot{\beta} &= 0.20127\alpha^2\beta - 0.0015591\alpha^2\mathrm{p} - 0.0021718\alpha^2\mathrm{r} + 0.0019743\alpha^2 x_c \\ &\quad + 0.32034\alpha\beta\mathrm{q} + 0.065962\beta^3 + 0.17968\alpha\beta + 0.98314\alpha\mathrm{p} - 0.023426\alpha\mathrm{r} \\ &\quad - 0.024926\alpha x_c + 0.134\beta\mathrm{q} + 0.0025822\alpha - 0.0068553\beta + 0.45003\mathrm{p} \\ &\quad + 0.1288\phi - 0.99443\mathrm{r} + 0.0056922 x_c\end{aligned}$$

$$\begin{aligned}\dot{\mathrm{p}} &= 17.7160\alpha^2\beta - 0.0277\alpha^2\mathrm{p} - 0.0386\alpha^2\mathrm{r} + 0.0351\alpha^2 x_c - 0.0033\beta^3 \\ &\quad + 2.1835\alpha\beta + 3.0420\alpha\mathrm{p} - 0.4139\alpha\mathrm{r} - 0.4699\alpha x_c - 0.8151\mathrm{qr} \\ &\quad - 0.0015\alpha - 3.7098\beta - 1.8607\mathrm{p} - 0.1096\mathrm{q} + 0.2799\mathrm{r} + 0.2723 x_c\end{aligned}$$

$$\begin{aligned}\dot{\mathrm{r}} &= -1.4509\alpha^2\beta + 0.0105\alpha^2\mathrm{p} + 0.0146\alpha^2\mathrm{r} - 0.0133\alpha^2 x_c + 0.0012\beta^3 \\ &\quad - 1.0095\alpha\beta - 0.0148\alpha\mathrm{p} + 0.1410\alpha\mathrm{r} + 0.1854\alpha x_c \\ &\quad - 0.7544\mathrm{pq} - 0.0185\alpha + 0.1620\beta + 0.0455\mathrm{p} - 0.2546\mathrm{r} - 0.1544 x_c\end{aligned}$$

$$\dot{\phi} = \mathrm{p}$$

$$\begin{aligned}\dot{\alpha} &= -\alpha\beta\mathrm{r} + 0.2467\alpha^2 - 0.1344\alpha\beta + 0.1473\alpha\mathrm{q} - \beta\mathrm{p} - 0.4538\beta\mathrm{r} - 0.2487\alpha \\ &\quad - 0.0609\beta + 0.7139\mathrm{q}\end{aligned}$$

$$\dot{\mathrm{q}} = 0.5196\alpha^2 + 4.8613\alpha\mathrm{q} + 0.97126\mathrm{pr} - 1.9162\alpha - 6.8140\mathrm{q} + 0.1305\mathrm{p}$$

$$\dot{x_c} = 4.9\mathrm{r} - x_c$$

2. Revised Closed Loop Model

$$\begin{aligned}\dot{\beta} = {} & 0.1831\alpha^2\beta - 0.0496\alpha^2\mathrm{p} - 0.0005\alpha^2\phi + 0.0017\alpha^2\mathrm{r} + 0.0030\alpha^2 x_c + 0.3203\alpha\beta\mathrm{q} \\ & + 0.0643\beta^3 + 0.0027\alpha\beta + 0.9557\alpha\mathrm{p} - 0.0054\alpha\phi + 0.0187\alpha\mathrm{r} - 0.0250\alpha x_c \\ & + 0.1340\beta\mathrm{q} + 0.0026\alpha - 0.0091\beta + 0.4457\mathrm{p} + 0.1276\phi - 0.9850\mathrm{r} + 0.0056 x_c\end{aligned}$$

$$\begin{aligned}\dot{\mathrm{p}} = {} & 1.1530\alpha^2\beta + 6.6577\alpha^2\mathrm{p} - 0.0082\alpha^2\phi + 0.0308\alpha^2\mathrm{r} - 0.1205\alpha^2 x_c + 18.3689\beta^3 \\ & - 0.5080\alpha\beta + 2.4908\alpha\mathrm{p} + 0.8743\alpha\phi - 7.2037\alpha\mathrm{r} - 0.3495\alpha x_c - 0.8151\mathrm{qr} \\ & - 0.0109\alpha - 4.6009\beta - 3.5186\mathrm{p} - 0.4703\phi - 0.1096\mathrm{q} + 3.9316\mathrm{r} + 0.2527 x_c\end{aligned}$$

$$\begin{aligned}\dot{\mathrm{r}} = {} & -1.4275\alpha^2\beta + 0.0546\alpha^2\mathrm{p} + 0.0031\alpha^2\phi - 0.0117\alpha^2\mathrm{r} - 0.0132\alpha^2 x_c \\ & + 0.0079\beta^3 - 1.0008\alpha\beta - 0.0096\alpha\mathrm{p} - 0.0029\alpha\phi + 0.1638\alpha\mathrm{r} + 0.1832\alpha x_c \\ & - 0.7544\mathrm{pq} - 0.0182\alpha + 0.1854\beta + 0.0895\mathrm{p} + 0.0124\phi - 0.3509\mathrm{r} - 0.1539 x_c\end{aligned}$$

$$\dot{\phi} = \mathrm{p}$$

$$\begin{aligned}\dot{\alpha} = {} & -\alpha\beta\mathrm{r} + 0.2467\alpha^2 - 0.1344\alpha\beta + 0.1473\alpha\mathrm{q} - \beta\mathrm{p} - 0.4538\beta\mathrm{r} - 0.2487\alpha \\ & - 0.0609\beta + 0.7139\mathrm{q}\end{aligned}$$

$$\dot{\mathrm{q}} = 0.5196\alpha^2 + 4.8613\alpha\mathrm{q} + 0.97126\mathrm{pr} - 1.9162\alpha - 6.8140\mathrm{q} + 0.1305\mathrm{p}$$

$$\dot{x_c} = 4.9\mathrm{r} - x_c$$